Check for updates

Journal of Intelligent Material Systems and Structures

Special Issue Article

Journal of Intelligent Material Systems and Structures
1–12
© The Author(s) 2018
Reprints and permissions:
sagepub.co.uk/journalsPermissions.nav
DOI: 10.1177/1045389X18758180
journals.sagepub.com/home/jim
SAGE

Core–skin debonding detection in honeycomb sandwich structures through guided wave wavefield analysis

Lingyu Yu[1], Zhenhua Tian[1], Xiaopeng Li[2], Rui Zhu[2] and Guoliang Huang[2]

Abstract

Ultrasonic guided waves have proven to be an effective and efficient method for damage detection and quantification in various plate-like structures. In honeycomb sandwich structures, wave propagation and interaction with typical defects such as hidden debonding damage are complicated; hence, the detection of defects using guided waves remains a challenging problem. The work presented in this article investigates the interaction of low-frequency guided waves with core–skin debonding damage in aluminum core honeycomb sandwich structures using finite element simulations. Due to debonding damage, the waves propagating in the debonded skin panel change to fundamental antisymmetric Lamb waves with different wavenumber values. Exploiting this mechanism, experimental inspection using a non-contact laser Doppler vibrometer was performed to acquire wavefield data from pristine and debonded structures. The data were then processed and analyzed with two wavefield data–based imaging approaches, the filter reconstruction imaging and the spatial wavenumber imaging. Both approaches can clearly indicate the presence, location, and size of the debonding in the structures, thus proving to be effective methods for debonding detection and quantification for honeycomb sandwich structures.

Keywords

Honeycomb sandwich, debonding detection, guided waves, wavenumber analysis

Introduction

Honeycomb sandwich structures have been increasingly used in aerospace, marine, and automotive applications since they have attractive features such as high strength/stiffness-to-weight ratio, acoustic insulation, noise control, and vibration damping (Bitzer, 1997; Fatemi and Lemmen, 2009; Vinson, 1999). However, honeycomb sandwich structures are susceptible to debonding damage along the core–skin interface, especially under intense dynamic or repetitive loading on the honeycomb core, due to weak shear strength of the bonding interface (Song et al., 2012). The debonding damage that occurs internally between the outer skin plate and the honeycomb core is not visible to the naked eye. However, the detection and quantification of such hidden damage are crucial, as the damage significantly impacts the integrity of the structure.

Ultrasonic guided waves have proven to be an effective and efficient method for damage detection and quantification due to their ability to propagate over long distances with less energy loss compared to bulk waves and their sensitivity to small structural defects (Giurgiutiu, 2008; Rose, 1999; Staszewski et al., 2004). They have been used extensively to detect defects such as cracks in metallic structures and delamination damage in laminated composites (Flynn et al., 2013; Hall

[1]Department of Mechanical Engineering, University of South Carolina, Columbia, SC, USA
[2]Department of Mechanical & Aerospace Engineering, University of Missouri, Columbia, MO, USA

Corresponding author:
Lingyu Yu, Department of Mechanical Engineering, University of South Carolina, Columbia, SC 29208, USA.
Email: yu3@cec.sc.edu

Guoliang Huang, Department of Mechanical & Aerospace Engineering, University of Missouri, Columbia, MO 65211, USA.
Email: huangg@missouri.edu

et al., 2011; He and Yuan, 2015; Jarmer et al., 2014; Kijanka et al., 2015; Moll et al., 2012; Tian et al., 2015b; Wang et al., 2004, 2015; Yu et al., 2013). In recent years, researchers have investigated the detection of debonding damage in honeycomb sandwich structures using guided waves (Baid et al., 2015; Chakraborty et al., 2012; Hosseini et al., 2014; Radzienski et al., 2016; Sikdar et al., 2015; Song et al., 2009, 2012; Tian et al., 2015a). Chakraborty et al. (2012) used guided waves to detect damage caused by low-velocity impacts in honeycomb sandwich structures where a monotonic amplitude increase in the reflection signal was observed with the increase in the damage size. Sikdar et al. (2015) studied guided wave propagation in a honeycomb sandwich composite with debonding damage and found that the group velocity of the A_0 mode increases with the increase in debonding size. Song et al. (2009) investigated guided wave propagation in honeycomb sandwich structures and found global guided waves in the sandwich at low frequencies and leaky guided waves from the skin plate to the honeycomb core. Recently, Radzienski et al. (2016) presented assessment of disbonding and crushed honeycomb core in composite sandwich panels based on anomalies of propagating guided waves acquired by laser vibrometry. They found that the excitation frequency significantly affects the imaging result and should be taken into account (Radzienski et al., 2016). These studies show that compared to simple metallic plates, honeycomb sandwich structures have more complex geometries, and thus more complicated guided wave characteristics. In addition, honeycomb sandwich structures can have hidden debonding damage present between the skin plate and the honeycomb core. Because of the complex wave propagation and interaction with damage in honeycomb sandwich structures, detecting and quantifying such hidden debonding damage using guided waves remain challenging tasks.

This article focuses on two aspects regarding (1) guided wave propagation in honeycomb sandwich structures to identify the appropriate excitation frequency and wave mode for core–skin debonding detection and (2) implementation of debonding detection through wavefield analysis and imaging. To investigate guided wave interaction with debonding damage, both finite element (FE) simulations and experimental inspection using laser vibrometry are performed. Wavefields acquired in the honeycomb structures with and without debonding damage (created by removing the adhesive film) are compared. Furthermore, the wavefields are transformed to the frequency–wavenumber spectra, which reveal intrinsic information for further comparison. Two wavefield imaging methods are implemented to discover the defects in the structure, including a filter reconstruction imaging and a spatial wavenumber imaging. The detection and quantification results clearly show the location, size, and shape of the debonding damage.

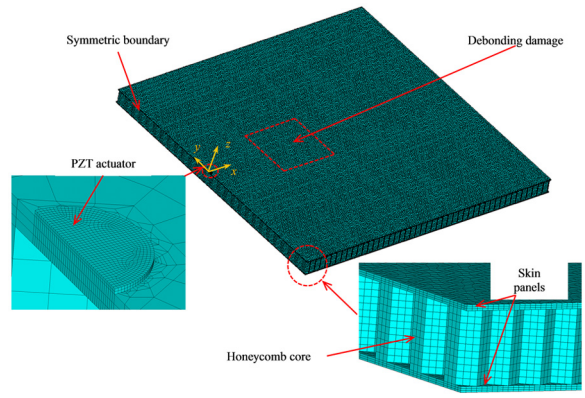

Figure 1. The finite element model of a honeycomb sandwich structure with a surface-bonded PZT actuator.

The remainder of this article is organized as follows: section "FE simulation" presents FE simulations of guided wave interaction with debonding damage in the honeycomb sandwich structure. Section "Experimental inspection" validates the simulation through laser vibrometry experiments. Section "Debonding detection and quantification" presents the frequency–wavenumber analysis and two imaging methods for debonding detection and quantification. Section "Conclusion" summarizes the findings and concludes the article.

FE simulation

Considering the complex geometries in honeycomb sandwich structures, FE method provides a practical and economical tool for predicting the guided wave propagation characteristics. The simulations are performed using the commercial software ANSYS/Multiphysics 15.0. Guided waves in honeycomb sandwich structures with and without debonding damage are simulated and compared. The effects of the debonding region size on the guided wave propagation are also investigated through FE simulations.

Simulation setup

The three-dimensional (3D) FE models for the honeycomb sandwich structures with and without debonding damage are established, as shown in Figure 1. The structure is composed of two outer skin plates and a hexagonal-celled core made of aluminum (elastic modulus 78 GPa, Poisson's ratio 0.33, and density 2730 kg/m^3). A piezoelectric (PZT) wafer, which is commonly used for guided wave generation nowadays, is bonded on the top surface of the structure. The geometric parameters are listed in Table 1. The material properties of the PZT actuator are assumed as

Table 1. Geometric parameters of the simulation (units: mm).

Skin plates			Honeycomb core			PZT actuator	
Length	Width	Thickness	Cell size	Wall thickness	Height	Diameter	Thickness
290	290	1	6.35	0.055	12.7	5	0.2

PZT: piezoelectric.

$$[\varepsilon] = \begin{bmatrix} 8.39 & 0 & 0 \\ & 8.39 & 0 \\ & \text{Symmetry} & 5.36 \end{bmatrix} \times 10^{-9}\ \mathrm{CV^{-1} \cdot m^{-1}}$$

$$[e] = \begin{bmatrix} 0 & 0 & -8.02 \\ 0 & 0 & -8.02 \\ 0 & 0 & 18.31 \\ 0 & 0 & 0 \\ 0 & 12.84 & 0 \\ 12.84 & 0 & 0 \end{bmatrix} \mathrm{C \times m^{-2}}$$

and

$$[c] = \begin{bmatrix} 97 & 49 & 44 & 0 & 0 & 0 \\ & 97 & 44 & 0 & 0 & 0 \\ & & 84 & 0 & 0 & 0 \\ & & & 22 & 0 & 0 \\ & & & & 24 & 0 \\ & & \text{Symmetry} & & & 24 \end{bmatrix} \times 10^{9}\ \mathrm{Pa}$$

where $[\varepsilon]$ is the dielectric matrix, $[e]$ is the PZT matrix, and $[c]$ is the stiffness matrix. The mass density of the PZT actuator is assumed to be 7700 $\mathrm{kg \times m^{-3}}$.

In the FE model, SOLID45 element with eight nodes having 3 degrees of freedom (DOFs) at each node is selected for the two outer skin plates. To model the honeycomb core with hexagonal cells, SHELL63 element with four nodes and 6 DOFs at each node is used. SHELL63 element allows for explicit numerical modeling with the exact hexagonal core geometry and provides enhanced accuracy for simulating guided waves with small wavelengths. The coupled field element SOLID5 with eight nodes and 6 DOFs at each node is selected to construct the PZT actuator. At the bottom nodes of the PZT actuator, a zero voltage is assigned as the electrical grounding. At the top nodes of the PZT actuator, an input voltage signal is applied to excite the PZT actuator. The coupled field modeling allows for precise PZT excitation and will provide higher precision compared to the simulation implemented by force or moment couples. A symmetric boundary condition is applied on all the nodes on the symmetric plane to reduce the computational demand.

The transient analysis is performed to simulate the guided wave propagation in the sandwich structure. To ensure the convergence of the transient analysis, the mesh element size needs to be fine enough, so that there are at least 10 elements per wavelength. Moreover, the integration time step should be small enough to ensure stability during the transient analysis (Song et al., 2009). To avoid boundary reflections, the sandwich structure needs to be long enough in the propagation direction. We find that the size of 290 mm × 290 mm is able to ensure the purity of the guided waves in this study. For the damage, a debonding defect under the top skin plate 50 mm away from the origin is included, as shown in Figure 1 (indicated by the red doted square). This debonding defect is numerically modeled by removing the constraint condition between the nodes in the skin plate and the sandwich core.

Simulation results

To investigate the effect of frequency on wave propagation, guided waves in a pristine honeycomb sandwich structure at three frequencies of 15, 50, and 100 kHz are simulated. Figure 2 presents the simulation results of displacements in the z-direction. At the low frequency of 15 kHz, the wavefield shows that global guided waves propagate in the entire sandwich. These global guided waves have large wavelengths and elliptical wavefronts. In this case, the entire sandwich can be considered as a solid waveguide that supports the global guided waves. At 50 kHz, although the global guided waves can still be observed, their wavefronts become closer to circular shapes other than elliptical shapes. At high frequency of 100 kHz, the global guided waves disappear. There are guided waves propagating in skin plates with circular wavefronts. Moreover, the result at 100 kHz shows complex speckle patterns that are induced by the wave interaction with the inside honeycomb core. Considering the very complex wave propagation at high frequency such as 100 kHz, low-frequency global guided waves will therefore be used to further investigate the wave interaction with core–skin debonding damage.

To study debonding effects on guided wave propagation, three cases with different debonding sizes (29 mm × 29 mm, 58 mm × 58 mm, and 85 mm × 85 mm) are simulated and compared to a pristine case. The wavefields at two time steps of 60 and 110 μs (before and after the waves arrive at the damage) at 40 kHz excitation are plotted in Figure 3. At 60 μs, the wavefields in the pristine structure (Figure 3(a)) and

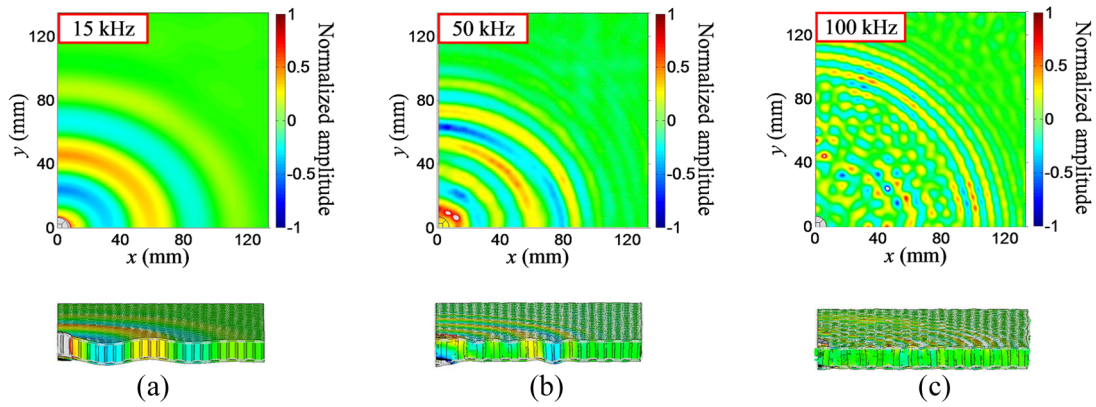

Figure 2. Simulation results (displacements in the z-direction) in the pristine sandwich: (a) top and front views at 15 kHz excitation, (b) top and front views at 50 kHz excitation, and (c) top and front views at 100 kHz excitation.

structures with different debonding defects (Figure 3(c), (e), and (g)) are nearly the same, and all show strong incident guided waves generated by PZT actuators. Since guided waves arrive at the left boundary of debonding at 60 μs, no wave reflections/interactions are observed. In our previous study, we found that guided waves excited in the frequency range of 15–50 kHz are global guided waves (Tian et al., 2015a). Hence, the guided waves at 40 kHz in this study are global guided waves in the entire cross section of the sandwich and have a long wavelength of 19 mm, which is about three times larger than a unit cell in the honeycomb core.

At 110 μs, the incident global guided waves arrive at the debonding defects, and strong wave interactions with the debonding defects are clearly demonstrated in the simulation results (Figure 3(d), (f), and (h)). With the increase in the debonding area, the area of wave interaction gradually increases. It is observed that wave reflections due to debonding defects are barely noticeable in the wavefield, and thus it is difficult to use the wave reflections for determining the debonding location and size. Nevertheless, waves propagating through the debonding area manifest very strong strengths compared to the waves in the pristine case. This implies that the transmitted waves can be used for the estimation of debonding location and size. This is expected because wave energy leaking from the top skin plate to the honeycomb core becomes smaller due to the presence of debonding. Hence, most wave energy is in the top skin plate. Note that in the debonding area, waves are propagating in the thin top skin plate as the A_0 Lamb mode. It is also noticed that the waves in the debonding area propagate faster compared to those in the pristine sandwich structure. This indicates that the A_0 mode Lamb waves in the debonding area of the top skin plate have a larger group velocity than the global guided wave in the sandwich.

Experimental inspection

Experimental studies of wave interaction with debonding damage in honeycomb sandwich structures have also been conducted using a surface-bonded PZT patch to generate guided waves and a non-contact scanning laser Doppler vibrometer (SLDV) to measure the wavefields.

Experimental setup

Two honeycomb sandwich structures with the same dimensions (305 mm × 305 mm × 15 mm) and same compositions (aluminum T3003 skin plates and a hexagonal-celled aluminum T3003 core) are used in the experiments. One structure has no debonding damage, while the other contains debonding damage with dimensions of 58 mm × 58 mm created by removing the adhesive film during the manufacturing process. The geometric parameters of the structures are listed in Table 2.

Figure 4 provides a schematic of the experimental setup, in which a PZT patch (APC 851: 7 mm diameter, 0.2 mm thickness) is bonded on the top surface of the structure to generate guided waves. The excitation signal is generated by a function generator (Hewlett Packard 33120A), amplified to 40 V by a voltage amplifier (Krohn-Hite 1506), and then applied to the PZT actuator. An SLDV (Polytec PSV-400-M2) is used to acquire the wavefield of guided waves. The laser beam is set normal to the specimen surface such that only the out-of-plane wave velocities are measured. The SLDV takes measurements point-by-point with a spatial resolution of 0.2 mm in a scanning area of 150 mm × 150 mm. At each point, the measurement is averaged 30 times to improve the signal-to-noise ratio. By measuring all the points in the scanning area, a wavefield in the form $v(t, \mathbf{x})$ as a function of both time t and space $\mathbf{x}$ is obtained (Yu and Tian, 2013).

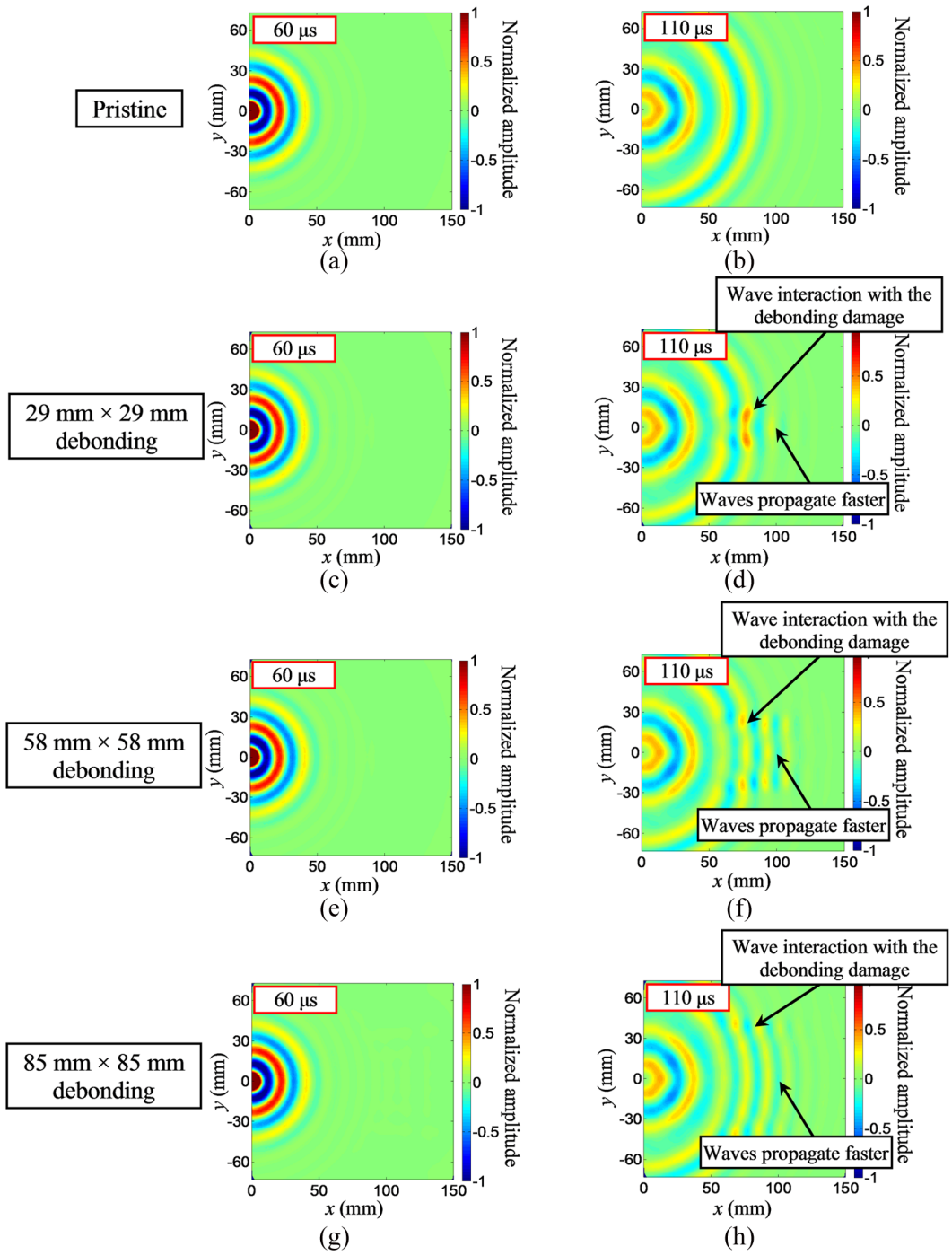

Figure 3. Simulation results (out-of-plane displacement wavefields) at 60 μs (left) and 110 μs (right) for 40 kHz excitation: (a) and (b) pristine sandwich structure, (c) and (d) 29 mm × 29 mm debonding, (e) and (f) 58 mm × 58 mm debonding, and (g) and (h) 85 mm × 85 mm debonding.

Table 2. Geometry parameters of honeycomb sandwiches (units: mm).

Skin plates			Honeycomb core			Debonding damage	
Length	Width	Thickness	Cell size	Wall thickness	Height	Length	Width
305	305	1	6.35	0.055	12.7	58	58

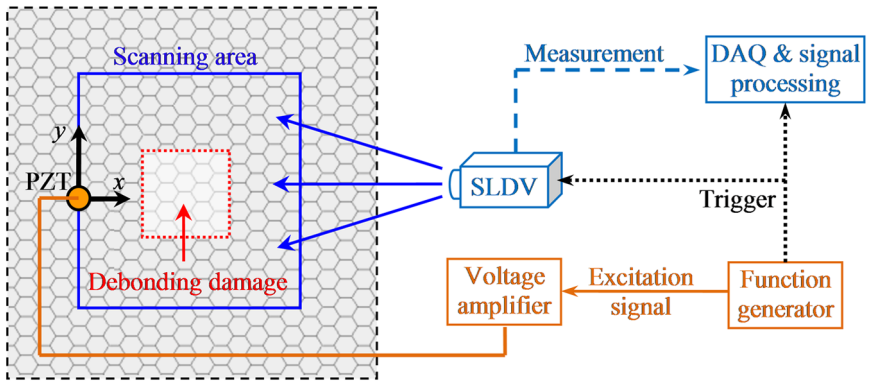

Figure 4. A schematic of the experimental setup.

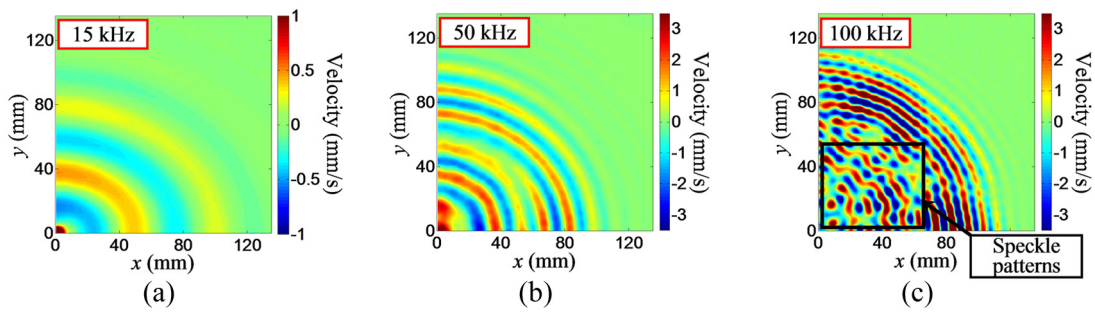

Figure 5. Experimental results (out-of-plane velocities) for the pristine honeycomb sandwich at (a) 15 kHz, (b) 50 kHz, and (c) 100 kHz, respectively.

Experimental results

Figure 5(a) to (c) are the experimental results in the pristine honeycomb sandwich at three different excitation frequencies of 15, 50, and 100 kHz, respectively. At very low frequency of 15 kHz, guided waves in the honeycomb sandwich have elliptical wavefronts and larger wavelengths. When the frequency goes higher from 15 to 100 kHz, the wavefronts in the honeycomb sandwich gradually change from elliptical fronts to circular fronts, and the wavelengths in the honeycomb sandwich become smaller. At 100 kHz, the wavefronts in the honeycomb sandwich become circular, and the wavefield shows speckle patterns that might be induced by the wave interaction with the inside honeycomb core. These experimental results agree well with the simulation results in Figure 2.

The wavefield comparison in the space domain shows interesting results. To further understand the guided waves in the honeycomb sandwich, the wavefields are transformed into the wavenumber domain, where the intrinsic wavenumber information of guided waves can be investigated. By applying 3D Fourier transform (FT), the time–space wavefields are transformed to the frequency–wavenumber spectra for further study. Figure 6(a) to (c) are the wavenumber spectra at 15, 50, and 100 kHz, respectively. The spectrum at 15 kHz shows an elliptical ring–shaped wavenumber band, which has smaller wavenumbers than the plate A_0 mode (represented by the solid line). With the increase in frequency from 15 to 100 kHz, the wavenumber band expands and the wavenumber values increase. Moreover, the elliptical ring–shaped wavenumber band gradually gets closer to the wavenumber curve of the plate A_0 mode. The comparison in Figure 6 shows that guided waves in the honeycomb sandwich have different wavenumbers compared to the A_0 waves in the skin plate, and with the increase in wave frequency, the wavenumber in the honeycomb sandwich is gradually asymptotic to that in the skin plate. Since low-frequency guided waves have simpler wavefields and larger wavenumber differences (between the honeycomb sandwich and the skin plate), the low-frequency guided waves (in the range 15–50 kHz) are the preferred waves for detecting core–skin debonding damage through wavefield analysis. Hence, the interaction of low-frequency guided waves with debonding damage is investigated.

Figure 7 compares the measured guided wavefields at 40 kHz in the pristine and debonded sandwich structures. At 60 μs, guided waves propagate in both sandwiches exhibiting identical wavefields (Figure 7(a) and (c)) prior to arrival at the debonding area. At 110 μs,

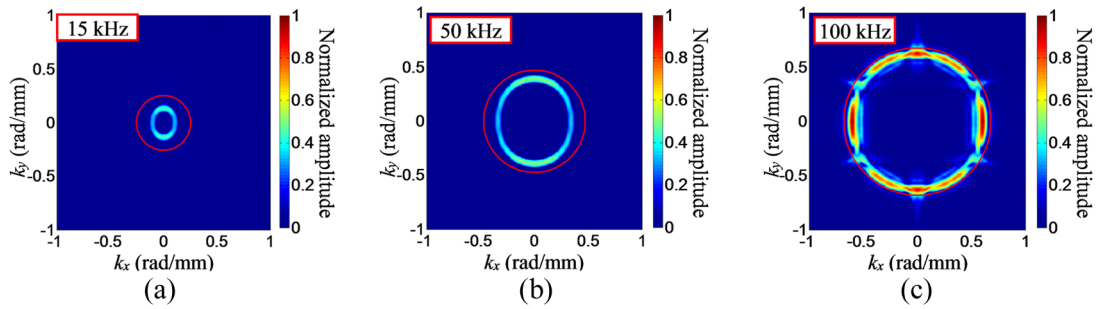

Figure 6. Wavenumber spectra corresponding to the wavefields in the pristine sandwich at (a) 15 kHz, (b) 50 kHz, and (c) 100 kHz. The solid line represents the theoretical wavenumber curves of the A_0 mode in a single skin plate. The wavenumber spectra are generated from the experimental wavefields through frequency–wavenumber analysis and symmetric expansion.

guided waves impinge the defect boundary and start interacting with the debonding in the damaged sandwich structures. Compared with the pristine structure (Figure 7(b)), the waves in the damaged structures (Figure 7(d)) show strong wave distortions due to the debonding damage. Wavefields (Figure 7) measured in the experiment agree well with the simulation results (Figure 3). In addition, both results show strong wave interactions, higher wave strength, and faster propagation speeds in the debonding area.

Debonding detection and quantification

Wavefields in Figure 7 show strong wave interactions in the debonding area indicating the presence of damage. However, neither characterization nor quantification of the wave interactions is available from the wavefields immediately. Hence, the wavefields are converted into the frequency–wavenumber domain where additional information about wave modes and wavenumber distributions can be obtained (Michaels et al., 2011; Ruzzene, 2007). The debonding effects on guided waves are analyzed by comparing the wavenumbers of the pristine and defect-present cases. Moreover, to detect and quantify debonding damage, two imaging methods based on wavenumber information are applied, including a filter reconstruction imaging and a spatial wavenumber imaging.

Frequency–wavenumber analysis

The time–space domain wavefield $v(t, \mathbf{x})$ can be transformed to a representation in the frequency–wavenumber domain using the multi-dimensional FT (Johnson and Dudgeon, 1993; Tian and Yu, 2014), given as

$$V(f, \mathbf{k}) = \int_{-\infty}^{\infty}\int_{-\infty}^{\infty}\int_{-\infty}^{\infty} v(t, \mathbf{x}) e^{-j(2\pi f t - \mathbf{k}\cdot\mathbf{x})} dt d\mathbf{x} \qquad (1)$$

where the space vector $\mathbf{x}$ and wavenumber vector $\mathbf{k}$ are defined as (x, y) and (k_x, k_y), respectively. $V(f, \mathbf{k})$ is the resulting frequency–wavenumber representation or "spectrum" in terms of frequency f and wavenumber vector $\mathbf{k}$. As frequency is the counterpart of time, wavenumber is the counterpart of spatial dimension. From spectrum $V(f, \mathbf{k})$, a wavenumber spectrum $V(f_0, \mathbf{k})$ at a specified frequency f_0 can be readily obtained. Details of the frequency–wavenumber domain analysis can be found in our previous publication (Tian and Yu, 2014).

Figure 8(a) and (b) shows wavenumber spectra at 40 kHz excitation frequency for the pristine and damaged honeycomb sandwich structures, respectively. Compared to the spectrum for the pristine sandwich in Figure 8(a), the spectrum for the damaged structure in Figure 8(b) shows additional wavenumber components, in addition to the changes in intensities. These additional wavenumber components have relatively larger values than those of the pristine sandwich, which might be related to the waves induced by the debonding damage.

Filter reconstruction imaging

The additional wavenumber components identified in the debonded sandwich structure are speculated as being related to the new waves induced by the debonding damage. To investigate the relation between the additional wavenumber components and the possible physical cause (debonding damage), a filtering technique is applied to acquire and study the additional wavenumber components shown in Figure 8(b).

Similar to digital filtering (Oppenheim et al., 1997), the filtering process of the wavenumber spectrum is mathematically expressed as a product between the frequency–wavenumber spectrum $V(f, \mathbf{k})$ and a band-pass filter function $F(\mathrm{f}, \mathbf{k})$ as

$$V_F(f, \mathbf{k}) = V(f, \mathbf{k}) F(f, \mathbf{k}) \qquad (2)$$

where $V_F(f, \mathbf{k})$ is the resulting spectrum. Since only the additional wavenumbers in Figure 8(b) are desired, a wavenumber filter is designed to retain only the additional wavenumber components and remove the rest.

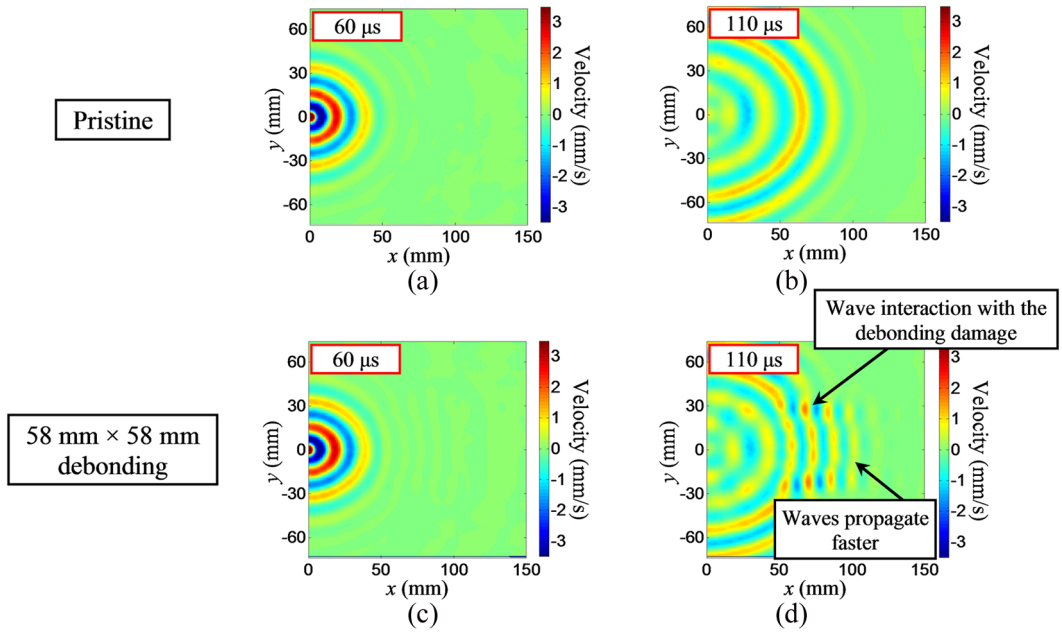

Figure 7. Experimental results (out-of-plane velocities) at 60 and 110 µs with 40 kHz excitation: (a) and (b) are for the pristine honeycomb sandwich structure; while (c) and (d) are for the structure with 58 mm × 58 mm debonding damage.

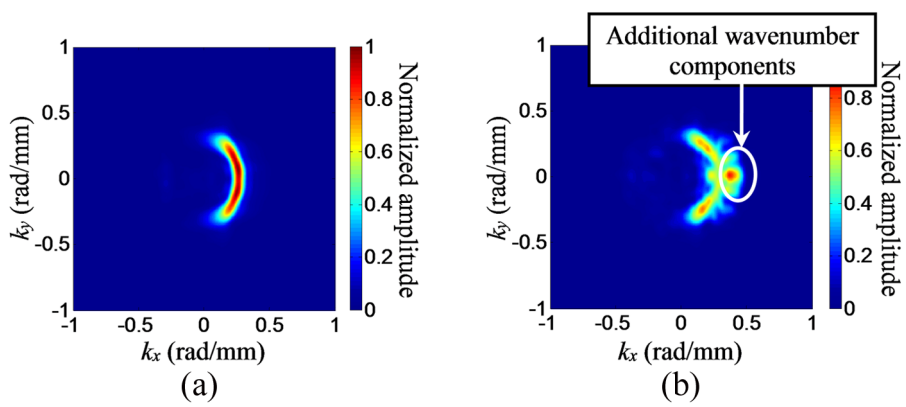

Figure 8. Wavenumber analysis of experimental results: (a) wavenumber spectrum for the pristine sandwich and (b) wavenumber spectrum for the sandwich with debonding damage.

In this study, the filter design is based on the wavenumber spectrum $V_P(f, \mathbf{k})$ of the pristine sandwich as

$$F(f, \mathbf{k}) = \begin{cases} 0 & \text{if } V_P(f, \mathbf{k}) > \text{threshold} \\ 1 & \text{otherwise} \end{cases} \tag{3}$$

In equation (3), when the amplitude of the pristine spectrum $V_P(f, \mathbf{k})$ is larger than the threshold, the filter value is set to 0. Otherwise, the filter value is set to 1. Figure 9(a) shows a wavenumber filter generated from the pristine spectrum (Figure 8(a)) with a threshold of 5%. By multiplying the filter with the spectrum of the damaged case (Figure 8(b)), a filtered spectrum (Figure 9(b)) is obtained, with only the additional wavenumber components.

Then, the filtered wavenumber spectrum $V_F(f, \mathbf{k})$ is reversed back to the time–space wavefield by applying the inverse 3D FT, as

$$v_F(t, \mathbf{x}) = \frac{1}{(2\pi)^2} \int_{-\infty}^{\infty} \int_{-\infty}^{\infty} \int_{-\infty}^{\infty} V_F(f, \mathbf{k}) e^{j(2\pi f t - \mathbf{k}\cdot\mathbf{x})} df d\mathbf{k} \tag{4}$$

Since the filtered spectrum $V_F(f, \mathbf{k})$ contains only the additional wavenumber components, the resulting wavefield $v_F(t, \mathbf{x})$ is equivalent in the time–space domain. Figure 9(c) plots the filtered wavefield at 110 µs, mainly in the area with debonding damage (dotted box). It shows that the additional wavenumber components are related to waves confined in the debonding area.

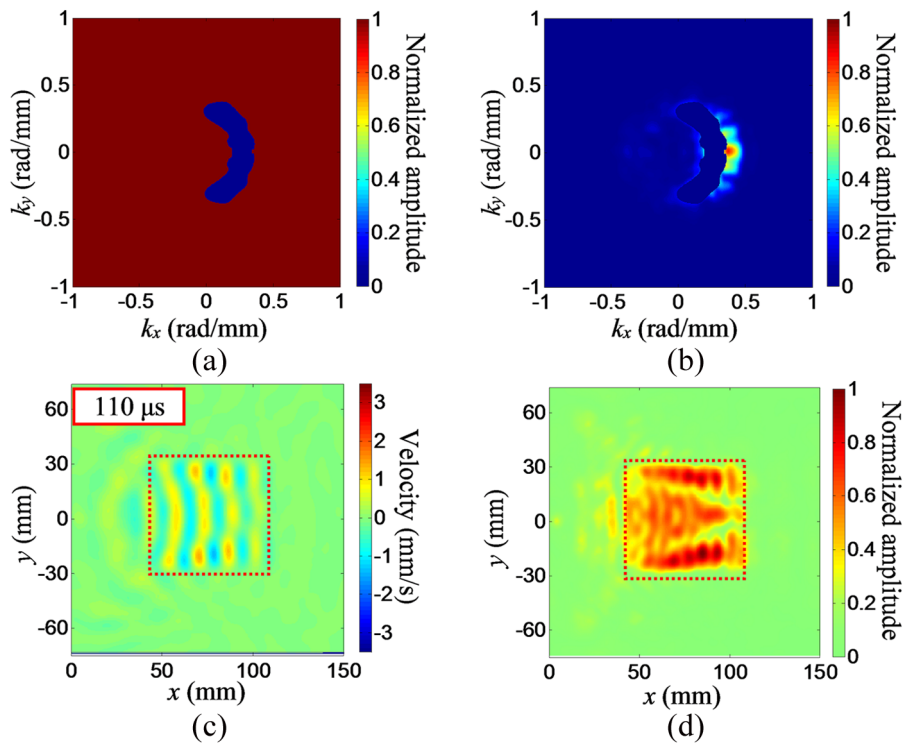

Figure 9. Filter reconstruction imaging results: (a) wavenumber filter, (b) filtered wavenumber spectrum, (c) reconstructed wavefield at 110 μs that corresponds to the spectrum in (b), and (d) energy map of the reconstructed wavefield. The dotted boxes in (c) and (d) represent the area of actual debonding damage.

Using the filtered time–space wavefield $v_F(t, \mathbf{x})$, a map of the cumulative wave energy (An et al., 2013; Kudela et al., 2015; Ostachowicz et al., 2014; Sohn et al., 2011) of the debonding-induced waves can be generated, as

$$E_F(\mathbf{x}, t) = \int_0^t \frac{1}{2} v_F^2(\tau, \mathbf{x}) d\tau \tag{5}$$

The resulting wave energy map is given in Figure 9(d), showing an area with high energy concentration, which matches well the actual debonding area (the dotted box). The energy map generated from the filtered wavefields can be used to locate and roughly quantify the size and shape of the debonding damage in the honeycomb sandwich structure.

Spatial wavenumber imaging

The results in the previous section prove that the filter reconstruction imaging is an effective method for quantifying the debonding damage. However, the design of the wavenumber filter requires the pristine wavenumber spectrum be obtained first. Another method, spatial wavenumber imaging, is developed to quantify the debonding damage for the case when the pristine spectrum is not available. The wavenumber imaging approach is based on *short-space* 3D FT and can generate an image in the present state (damaged structure) without information from the prior state (pristine). The spatial wavenumber imaging can always provide an additional means to evaluate the debonding for enhanced reliability and robustness of the damage characterization.

Short-space 3D FT is a spatially windowed FT by applying a sliding window along the spatial dimension (Rogge and Leckey, 2013; Tian et al., 2015b), and the result can indicate how the frequency and/or wavenumber components vary in space. Through the transformation, a coupled space-frequency–wavenumber representation $S(\bar{\mathbf{x}}, f, \mathbf{k})$ can be obtained, as

$$S(\bar{\mathbf{x}}, f, \mathbf{k}) = \int_{-\infty}^{\infty}\int_{-\infty}^{\infty}\int_{-\infty}^{\infty} v(t, \mathbf{x}) W(\mathbf{x} - \bar{\mathbf{x}}) e^{-j(2\pi f t - \mathbf{k}\cdot\mathbf{x})} dt d\mathbf{x} \tag{6}$$

where $\bar{\mathbf{x}}$ is the retained spatial vector $(\bar{x}, \bar{y})$, and $W(\mathbf{x})$ is a spatial window function. In our application, a Hanning function is selected to construct the window function $W(\mathbf{x})$, given as

$$W(\mathbf{x}) = \begin{cases} 0.5\left[1 + \cos\left(2\pi \frac{|\mathbf{x}|}{D_x}\right)\right] & \text{if } |\mathbf{x}| \le D_x/2 \\ 0 & \text{otherwise} \end{cases} \tag{7}$$

where D_x is the window length in the space domain. By sliding the window $W(\mathbf{x})$ along the spatial dimension, a space–frequency–wavenumber representation $S(\bar{\mathbf{x}}, f, \mathbf{k})$ can be obtained.

Using $S(\bar{\mathbf{x}}, f, \mathbf{k})$, we define a new spatial wavenumber function $k_{sw}(\bar{\mathbf{x}}, f)$, by finding the wavenumber, at which the representation $S(\bar{\mathbf{x}}, f, \mathbf{k})$ has the largest amplitude, as

$$k_{sw}(\bar{\mathbf{x}}, f) = |\mathbf{k}_{sw}(\bar{\mathbf{x}}, f)| \tag{8}$$

where

$$\mathbf{k}_{sw}(\bar{\mathbf{x}}, f) = \arg\max_{\mathbf{k}} |S(\bar{\mathbf{x}}, f, \mathbf{k})| \tag{9}$$

It should be noted that no real signal has a singular frequency component. Hence, equation (8) is further optimized by taking the average spatial wavenumber $k_{sw}(\bar{\mathbf{x}})$, over a selected frequency range, given as

$$k_{sw}(\bar{\mathbf{x}}) = \frac{1}{N}\sum_{i=1}^{N} k_{sw}(\bar{\mathbf{x}}, f_i) \tag{10}$$

where f_i ($i = 1, 2, 3, \ldots, N$) are the frequencies within the selected frequency bandwidth Δf. The resulting spatial wavenumber $k_{sw}(\bar{\mathbf{x}})$ is then mapped as an intensity image representing how the wavenumbers within the selected frequency band are distributed along spatial dimensions.

Using the wavenumber imaging defined by equations (8) to (10), Figure 10 presents the image generated over the frequency band 35–45 kHz for the sandwich structure with debonding damage. The intensity indicates an area approximately 55 mm × 60 mm in size. This area has significantly larger wavenumbers than the rest area, for the reason that A_0 mode in the debonding region has larger wavenumbers than global guided waves in the rest area. The detected location and the quantified size of the debonding damage agree well with the location and the size of the actual debonding damage (indicated by the dotted box) in the sandwich structure. This provides strong evidence that our approach can be used for not only detecting but also quantifying possible debonding damage in honeycomb sandwich structures.

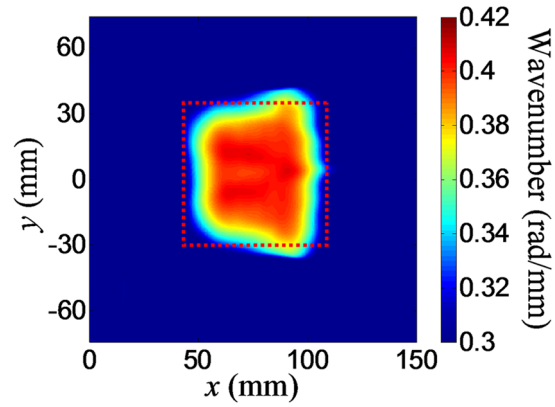

Figure 10. Debonding detection and quantification using spatial wavenumber imaging. The dotted box represents the area of actual debonding damage.

Conclusion

This article presents a fundamental study of guided wave propagation in honeycomb sandwich structures with core–skin debonding damage and the development of effective damage imaging approaches for the debonding detection and characterization. Through FE simulations, guided waves in sandwich structures with core–skin debonding damage are compared to those in a pristine structure. The comparison shows that guided waves change to a fundamental A_0 Lamb mode in the debonding region at low frequencies. This mode conversion in the debonding area generates a larger wavenumber compared to the wavenumber of original waves before mode conversion. Thus, the mode conversion offers useful information for detecting the debonding damage. Based on this mechanism, imaging methods for the detection of debonding damage are developed. The imaging methods use multi-dimensional wavefield data acquired by a non-contact SLDV system. The non-contact nature of the sensing system is non-invasion to the inspected structures and significantly reduces the labor of sensor installation and maintenance. Moreover, the measured wavefield data provide immediate preliminary information regarding the structural integrity. The intrinsic characterization of waves in the honeycomb sandwich structures is further performed using the multi-dimensional FT to obtain the frequency–wavenumber information.

To detect and quantify the debonding damage, two imaging methods are developed. The filter reconstruction imaging makes use of the additional wavenumbers exhibited in the debonded plate and converts them back to the time–space domain to generate a map of wave energy. It has the advantage of being a quick method but requires the knowledge of pristine plate condition. The spatial wavenumber imaging approach calculates wavenumbers at each spatial location over a certain frequency band to generate the image. Although calculation-intensive, it does not require prior knowledge of the plate condition. Both approaches are applied to evaluate the core–skin debonding in this study and show consistent results, agreeing well with the actual defect. Our study not only shows that the wavefield-based imaging methods are promising for guided waves with larger wavelengths at lower frequencies compared to previous work at higher frequencies (Flynn et al., 2013; Yu et al., 2013) but also confirms their viability for core–skin debonding evaluation in honeycomb sandwich structures. Future work will include applying

this method for core–skin debonding defects with complex shapes and composite sandwich structures.

Declaration of conflicting interests

The author(s) declared no potential conflicts of interest with respect to the research, authorship, and/or publication of this article.

Funding

The authors would like to thank US Department of Energy (DOE) Office of Nuclear Energy under Grant No. DE-NE 0000726 and DE-NE 0008400 and Air Force Office of Scientific Research under Grant No. AF 9550-15-1-0016 with Program Manager Dr Byung-Lip (Les) Lee.

ORCID iDs

Lingyu Yu https://orcid.org/0000-0002-0514-5490
Zhenhua Tian https://orcid.org/0000-0002-1903-5604

References

An YK, Park B and Sohn H (2013) Complete noncontact laser ultrasonic imaging for automated crack visualization in a plate. *Smart Materials and Structures* 22: 025022.

Baid H, Schaal C, Samajder H, et al. (2015) Dispersion of Lamb waves in a honeycomb composite sandwich panel. *Ultrasonics* 56: 409–416.

Bitzer T (1997) *Honeycomb Technology: Materials, Design, Manufacturing, Applications and Testing*. Dordrecht: Springer.

Chakraborty N, Rathod VT, Mahapatra DR, et al. (2012) Guided wave based detection of damage in honeycomb core sandwich structures. *NDT & E International* 49: 27–33.

Fatemi J and Lemmen M (2009) Effective thermal/mechanical properties of honeycomb core panels for hot structure applications. *Journal of Spacecraft and Rockets* 46: 514–525.

Flynn EB, Chong SY, Jarmer GJ, et al. (2013) Structural imaging through local wavenumber estimation of guided waves. *NDT & E International* 59: 1–10.

Giurgiutiu V (2008) *Structural Health Monitoring with Piezoelectric Wafer Active Sensors*. Boston, MA: Academic Press.

Hall JS, McKeon P, Satyanarayan L, et al. (2011) Minimum variance guided wave imaging in a quasi-isotropic composite plate. *Smart Materials and Structures* 20: 025013.

He JZ and Yuan FG (2015) Damage identification for composite structures using a cross-correlation reverse-time migration technique. *Structural Health Monitoring* 14: 558–570.

Hosseini SM, Willberg C, Kharaghani A, et al. (2014) Characterization of the guided wave propagation in simplified foam, honeycomb and hollow sphere structures. *Composites Part B: Engineering* 56: 553–566.

Jarmer GJS, Flynn EB and Todd MD (2014) Multi-wave-mode, multi-frequency detectors for guided wave interrogation of plate structures. *Structural Health Monitoring* 13: 120–130.

Johnson DH and Dudgeon DE (1993) *Array Signal Processing: Concepts and Techniques*. Upper Saddle River, NJ: Prentice Hall.

Kijanka P, Manohar A, di Scalea FL, et al. (2015) Damage location by ultrasonic Lamb waves and piezoelectric rosettes. *Journal of Intelligent Material Systems and Structures* 26: 1477–1490.

Kudela P, Radzienski M and Ostachowicz W (2015) Identification of cracks in thin-walled structures by means of wavenumber filtering. *Mechanical Systems and Signal Processing* 50–51: 456–466.

Michaels TE, Michaels JE and Ruzzene M (2011) Frequency-wavenumber domain analysis of guided wavefields. *Ultrasonics* 51: 452–466.

Moll J, Torres-Arredondo MA and Fritzen CP (2012) Computational aspects of guided wave based damage localization algorithms in flat anisotropic structures. *Smart Structures and Systems* 10: 229–251.

Oppenheim AV, Willsky AS and Hamid S (1997) *Signals and Systems*. 2nd ed. Upper Saddle River, NJ: Prentice Hall.

Ostachowicz W, Radzienski M and Kudela P (2014) 50th anniversary article: comparison studies of full wavefield signal processing for crack detection. *Strain* 50: 275–291.

Radzienski M, Kudela P and Ostachowicz W (2016) Assessment of honeycomb core condition in composite sandwich panels by means of guided waves. In: *8th European workshop on structural health monitoring (EWSHM)*, Bilbao, 5–8 July 2016.

Rogge MD and Leckey CAC (2013) Characterization of impact damage in composite laminates using guided wavefield imaging and local wavenumber domain analysis. *Ultrasonics* 53: 1217–1226.

Rose JL (1999) *Ultrasonic Waves in Solid Media*. Cambridge: Cambridge University Press.

Ruzzene M (2007) Frequency-wavenumber domain filtering for improved damage visualization. *Smart Materials and Structures* 16: 2116–2129.

Sikdar S, Banerjee S and Ashish G (2015) Ultrasonic guided wave propagation and disbond identification in a honeycomb composite sandwich structure using bonded piezoelectric wafer transducers. *Journal of Intelligent Material Systems and Structures* 27: 1767–1779.

Sohn H, Dutta D, Yang JY, et al. (2011) Automated detection of delamination and disbond from wavefield images obtained using a scanning laser vibrometer. *Smart Materials and Structures* 20: 045017.

Song F, Huang GL and Hu GK (2012) Online guided wave-based debonding detection in honeycomb sandwich structures. *AIAA Journal* 50: 284–293.

Song F, Huang GL and Hudson K (2009) Guided wave propagation in honeycomb sandwich structures using a piezoelectric actuator/sensor system. *Smart Materials and Structures* 18: 125007.

Staszewski WJ, Boller C and Tomlinson GR (2004) *Health Monitoring of Aerospace Structures*. Chichester: John Wiley & Sons.

Tian ZH and Yu LY (2014) Lamb wave frequency-wavenumber analysis and decomposition. *Journal of Intelligent Material Systems and Structures* 25: 1107–1123.

Tian ZH, Yu LY, Huang GL, et al. (2015a) Wavenumber study of guided waves in aluminum honeycomb sandwich structures. In: *Health monitoring of structural and*

biological systems 2015, San Diego, CA, 8–12 March 2015,vol. 943807. San Diego, CA: SPIE Press.

Tian ZH, Yu LY, Leckey C, et al. (2015b) Guided wave imaging for detection and evaluation of impact-induced delamination in composites. *Smart Materials and Structures* 24: 105019.

Vinson JR (1999) *The Behavior of Sandwich Structures of Isotropic and Composite Materials*. Lancaster: Technomic Publishing Company.

Wang CH, Rose JT and Chang FK (2004) A synthetic time-reversal imaging method for structural health monitoring. *Smart Materials and Structures* 13: 415–423.

Wang Q, Hong M and Su ZQ (2015) An in-situ structural health diagnosis technique and its realization via a modularized system. *IEEE Transactions on Instrumentation and Measurement* 64: 873–887.

Yu L and Tian Z (2013) Lamb wave structural health monitoring using a hybrid PZT-laser vibrometer approach. *Structural Health Monitoring* 12: 469–483.

Yu L, Leckey CAC and Tian Z (2013) Study on crack scattering in aluminum plates with Lamb wave frequency-wavenumber analysis. *Smart Materials and Structures* 22: 065019.